

# Periodic spin textures in a degenerate $F = 1$ $^{87}\text{Rb}$ spinor Bose gas

M. Vengalattore<sup>1,\*</sup>, J. Guzman<sup>1</sup>, S. R. Leslie<sup>1</sup>, F. Serwane<sup>1</sup>, and D. M. Stamper-Kurn<sup>1,2†</sup>

<sup>1</sup>*Department of Physics, University of California, Berkeley CA 94720*

<sup>2</sup>*Materials Sciences Division, Lawrence Berkeley National Laboratory, Berkeley, CA 94720*

(Dated: October 27, 2018)

We report on the spin textures produced by cooling unmagnetized  $^{87}\text{Rb}$   $F = 1$  spinor gases into the regime of quantum degeneracy. At low temperatures, magnetized textures form that break translational symmetry and display short-range periodic magnetic order characterized by one- or two-dimensional spatial modulations with wavelengths much smaller than the extent of the quasi-two-dimensional degenerate gas. Spin textures produced upon cooling spin mixtures with a non-zero initial magnetic quadrupole moment also show ferromagnetic order that, at low temperature, coexists with the spatially modulated structure.

Coherent quantum fluids exhibiting spontaneous spatial order have garnered widespread attention in connection to possible supersolid phases of matter [1] and the ground states of high- $T_c$  superconductors [2, 3] and other correlated electronic materials [4]. Such intrinsically heterogeneous quantum fluids may arise due to the interplay between multiple order parameters [4], the influence of adjacent ground states with differing tendencies [5] or the presence of competing interactions [6, 7].

Recent observations hint at similar phenomenology in a magnetic quantum gas, the  $F = 1$  spinor Bose gas of  $^{87}\text{Rb}$ . Early studies of  $^{87}\text{Rb}$  spinor condensates [8, 9] suggested that their magnetic properties were governed solely by the spin-dependent contact interaction. This interaction, with mean-field energy  $-|c_2|n\langle\mathbf{F}\rangle^2$ , favors spin states with maximum magnetization [10, 11]; here,  $c_2$  is related to  $s$ -wave scattering lengths for interatomic collisions,  $n$  is the number density, and  $\mathbf{F}$  is the dimensionless vector spin. Together with the kinetic energy cost for spatial variation of the superfluid vector order parameter, this local interaction favors a simple, homogeneous, ferromagnetically ordered spinor condensate. However, recent works [12–15] point to the significance of magnetic dipolar interactions in determining magnetization dynamics in  $^{87}\text{Rb}$  gases with large spatial extent. This interaction is long-ranged and spatially anisotropic, and, as in magnetic thin films, may favor inhomogeneous and spatially ordered spin textures. How the competition between the spatially isotropic contact interaction and the anisotropic long-range dipole interaction resolves itself in such degenerate spinor gases is the subject of several recent theoretical investigations [16–20], and remains an open experimental question.

Here, we address this question by examining the magnetic order in gases produced upon cooling unmagnetized thermal spin mixtures into the regime of quantum degeneracy. At their lowest temperatures, these quantum fluids break translational symmetry to arrive at magnetized spin textures that, while varying between samples,

consistently display spatial modulations of similar morphology and length scale independent of initial conditions and equilibration time.

This work differs from previous studies of spin textures of spinor Bose condensates [15, 21, 22] (also for  $F = 2$  gases [23]) in two crucial respects. First, in previous works, modulated spin textures arose from dynamical instabilities of long-range-ordered spin-polarized Bose-Einstein condensates. Thus, the different characteristics of the magnetization structures observed in those works, while providing insight on the magnetic interactions present in the spinor gas, derived from the specific unstable initial states chosen. Indeed, the magnetization patterns produced through two different dynamic instabilities, the first being the spin-mixing instability of a paramagnetic condensate quenched across a phase transition [21, 22] and the second being an instability of a helical spin texture [15], showed markedly different spatial correlations. As such, the present study is aimed at revealing the magnetic phases favored intrinsically by the spinor gas. Second, this work presents the first observation of spin textures in degenerate Bose gases at variable temperature, whereas previous works examined structure formation only at near-zero temperature. The addition of a significant normal gas component should add new means for dissipation and relaxation from non-equilibrium magnetization states.

## I. EXPERIMENTAL METHOD

The local one-body density matrix of a spin-1 atomic gas describes both rank-1 and rank-2 polarization moments, corresponding to the vector spin and magnetic quadrupole moments of the atoms, respectively. For our experiments, we prepared non-degenerate optically trapped gases characterized by homogeneous fractional populations  $(\zeta_1, \zeta_0, \zeta_{-1})$  in the three eigenstates of  $F_z$ . These gases were unmagnetized, i.e. characterized by zero vector spin, given the dual constraints of  $\zeta_1 = \zeta_{-1}$  (zero longitudinal magnetization) and the absence of coherence among the sublevels (zero transverse magnetization). These constraints still allow for a non-zero rank-2 (magnetic quadrupole) polarization moment, for

\* Present address: Laboratory of Atomic and Solid State Physics, Cornell University, Ithaca, NY 14853.

† Electronic address: dmsk@berkeley.edu

$\eta = \zeta_0 - \zeta_1 \neq 0$ , which breaks spin-rotational symmetry by favoring the  $\hat{z}$  axis.

To prepare such spin mixtures, we began with non-degenerate, longitudinally spin-polarized gases trapped at the focus of an elliptically focused, linearly polarized, 825-nm wavelength laser beam. We then produced incoherent spin mixtures by applying resonant  $\pi/2$  rf pulses while also applying a 50 mG/cm magnetic field gradient to the gas. Diffusion of the non-degenerate atoms in the inhomogeneous field eliminated transverse coherences, as ascertained by probing for Larmor precession in the thermal gas [24]. Applying a single rf pulse resulted with an  $\eta = 1/4$  spin mixture, while applying the pulse-diffusion sequence repeatedly yielded a fully unpolarized gas with  $\eta = 0$ .

Following their preparation, spin mixtures were evaporatively cooled by gradually lowering the intensity of the optical trapping beam, typically over 200 ms. During this process, the trap frequencies, with values of  $(\omega_x, \omega_y, \omega_z) = 2\pi(84, 1000, 10) \text{ s}^{-1}$  at the initial trap depth of  $U/k_B \simeq 10 \mu\text{K}$ , decreased as  $\omega_{x,y,z} \propto \sqrt{U}$  and the gas temperature was found to scale as  $k_B T = 0.11(U/k_B - 0.8 \mu\text{K})$ , with all Zeeman sublevels attaining the same temperature. The offset in the formula for the temperature  $T$  accounts for the effects of gravity in the  $\hat{y}$  direction.

After the optical trap depth was reduced to the desired level, the spinor gas was allowed to equilibrate, typically for another 200 ms, and was then probed by either of two methods. The instantaneous vector magnetization  $\vec{M} = \mu \tilde{n} \mathbf{F}$ , column-integrated along the  $\hat{y}$  imaging axis, was measured in the  $\hat{x}$ - $\hat{z}$  plane by magnetization-sensitive phase contrast imaging, at a measured imaging resolution of about  $2 \mu\text{m}$  [24, 25]. Here,  $\mu$  is the atomic magnetic moment and  $\tilde{n}$  is the local column density of the gas. Alternately, to measure the temperature, atom number and condensate fraction for each of the Zeeman sublevels, the gas was released from the optical trap and subjected to a magnetic field gradient that served to separate spatially the three Zeeman states. The three components were then imaged following an additional time of flight (Fig. 1).

Throughout the evaporation and equilibration, a  $B = 150$  mG magnetic field, varying by less than  $5 \mu\text{G}$  across the extent of the gas, was applied along  $\hat{z}$ . This field produces a quadratic Zeeman shift of the form  $qF_z^2$  with  $q/h = (70 \text{ Hz/G}^2)B^2 = 1.5 \text{ Hz}$ . This shift is smaller than the spin-dependent contact and dipolar interactions in the degenerate gases studied, with typical energies of  $|c_2|n = h \times 7 \text{ Hz}$  and  $\mu_0 \mu^2 n = h \times 8 \text{ Hz}$ , respectively, at a typical density of  $n = 2 \times 10^{14} \text{ cm}^{-3}$ . The field also induces rapid (110 kHz) Larmor precession of the atomic spins, owing to which the magnetic dipole interactions assume a precession-averaged form [14, 15, 17].

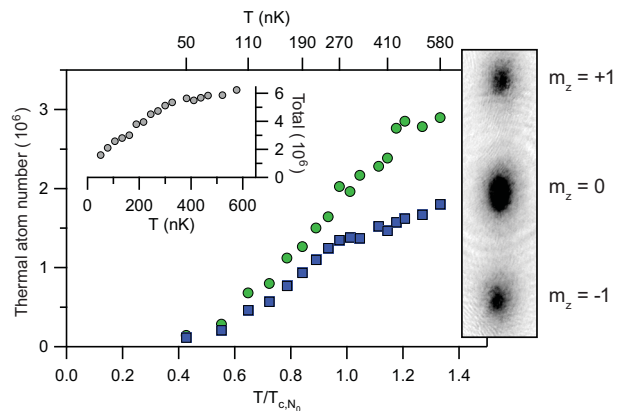


FIG. 1. The number of atoms in the thermal fraction of the  $|m_z = 0\rangle$  sublevel (green circles) is compared with the average number in the thermal fractions of the  $|m_z = \pm 1\rangle$  states (blue squares) at different final temperatures of the  $\eta = 1/4$  clouds. These data are derived from bimodal fits to time-of-flight density images taken after the three spin states were spatially separated in a magnetic field gradient (such an image is shown at right). While the relative populations in the Zeeman levels at high temperature are consistent with the initial value of  $\eta = 1/4$ , below  $T_{c,N_0}$ , the thermal components in all Zeeman components become roughly equal. A record of the total atom number (condensed and non-condensed) in all three sublevels vs. temperature is shown in the inset.

## II. MAGNETIZATION TEXTURES PRODUCED FROM $\eta = 0$ GASES

Spinor gases produced initially with  $\eta = 0$  correspond to the equilibrium state far from quantum degeneracy for our system where  $k_B T \gg \{q, |c_2|n\}$ . The bulk features of gases produced by cooling this initial mixture display several hallmarks of Bose condensation. Gases probed after a time of flight show the transition from a Bose-enhanced gaussian distribution to a bimodal density distribution at a temperature consistent with the ideal-gas Bose-Einstein condensation temperature,  $T_{c,N_0}$ , given as  $k_B T_{c,N_0} = \hbar \bar{\omega} (N_0/1.21)^{1/3}$  where  $\bar{\omega} = (\omega_x \omega_y \omega_z)^{1/3}$  and  $N_0$  is the atom number in the  $|m_z = 0\rangle$  state. The measured populations within the central peak and the gaussian distribution, associated typically with the condensate and thermal fractions, respectively, match closely with those expected for scalar Bose gases. The total population in each Zeeman sublevel remained roughly equal as the gas was cooled.

However, *in situ* probing of these gases (Fig. 2) reveals the formation of complex magnetic structure. Immediately below  $T_{c,N_0}$ , the spinor gas becomes spontaneously magnetized, breaking spin-rotational symmetry within a central region consistent with the spatial dimension of a Bose condensate. The magnetization observed for two samples produced under similar conditions is shown in Fig. 3. These inhomogeneous textures are dominated by strong modulation of the magnetization with a characteristic domain size  $l$  of about  $5 \mu\text{m}$ . We observed spin

domains of similar size even in gases with reduced atom number for which the condensate radii were roughly half those shown in Fig. 2. That this length  $l$  is smaller than the condensate dimensions in the imaged  $\hat{x}$ - $\hat{z}$  plane and is not strongly dependent on the  $\hat{x}$  dimension of the condensate suggests that the observed translational symmetry breaking is an intrinsic tendency of this quantum gas.

We note also that both  $l$  and also the spin healing length defined as  $\xi_s = \hbar/(2m|c_2|n)^{1/2} = 3 \mu\text{m}$  exceed the Thomas-Fermi condensate radius along the direction of tightest confinement,  $r_y \simeq 1.5 \mu\text{m}$ . Thus, spin textures of the degenerate gas may be considered two-dimensional. In contrast, the scalar healing length, defined conventionally as  $\xi = \hbar/(2mc_0n)^{1/2} = 0.2 \mu\text{m}$  with  $c_0$  defining the spin-independent contact interaction strength, is smaller than the Thomas-Fermi radii of the condensate. Thus, in terms of scalar excitations, the degenerate gas may be considered three-dimensional.

Importantly, these textures display spatial order, characterized by strong modulation along two distinct wavevectors. To illustrate this spatial order, we consider the spatial correlation function of the vector magnetization, defined as

$$G(\delta\mathbf{r}) = \frac{\sum_{\mathbf{r}} \tilde{\mathbf{M}}(\mathbf{r} + \delta\mathbf{r}) \cdot \tilde{\mathbf{M}}(\mathbf{r})}{\mu^2 \sum_{\mathbf{r}} \tilde{n}(\mathbf{r} + \delta\mathbf{r}) \tilde{n}(\mathbf{r})} \quad (1)$$

and shown in Fig. 3. The characteristic spatial pattern is indicated by the lobes of positive and negative spin correlation surrounding the central region of positive correlation at  $\delta\mathbf{r} = \mathbf{0}$ . This spatial organization is equivalently indicated by peaks in the Fourier power spectrum of the vector magnetization,  $|\tilde{\mathbf{M}}(k_x, k_z)|^2$ , at wavevectors  $k \simeq \pi/l$  (Fig. 4) [26]. We highlight three characteristics of this spatial order. First, the alternating domain pattern is short-ranged, extending regularly only over a typical range of  $30 \mu\text{m}$  that is much shorter than the maximum extent ( $\simeq 300 \mu\text{m}$  at low temperatures) of the magnetized degenerate gas. Second, the modulation pattern varies visibly between samples produced at similar temperatures and equilibration times, with the spin texture in some regions characterized by a checkerboard, or two-wavevector pattern of magnetization, while in other regions the modulation along one wavevector appears more dominant. In spite of these variations, the orientation of the two modulation wavevectors is fairly constant across samples. We observe that a rotation of the optical trap about  $\hat{y}$  causes a corresponding rotation in the crystal wavevectors, demonstrating that the orientation of the magneto-crystalline pattern in the  $\hat{x}$ - $\hat{z}$  plane is pinned to the boundaries imposed by the trap. We cannot account for a misalignment of these wavevectors from the apparent trap axes, though we suspect it arises from trap asymmetries due to aberrations in the optical trapping laser beam.

Third, the magnetization modulation of these spin textures is characterized by an axis in spin space along which the magnetization exhibits the largest variance. To identify this local spin axis, we considered the distribution of

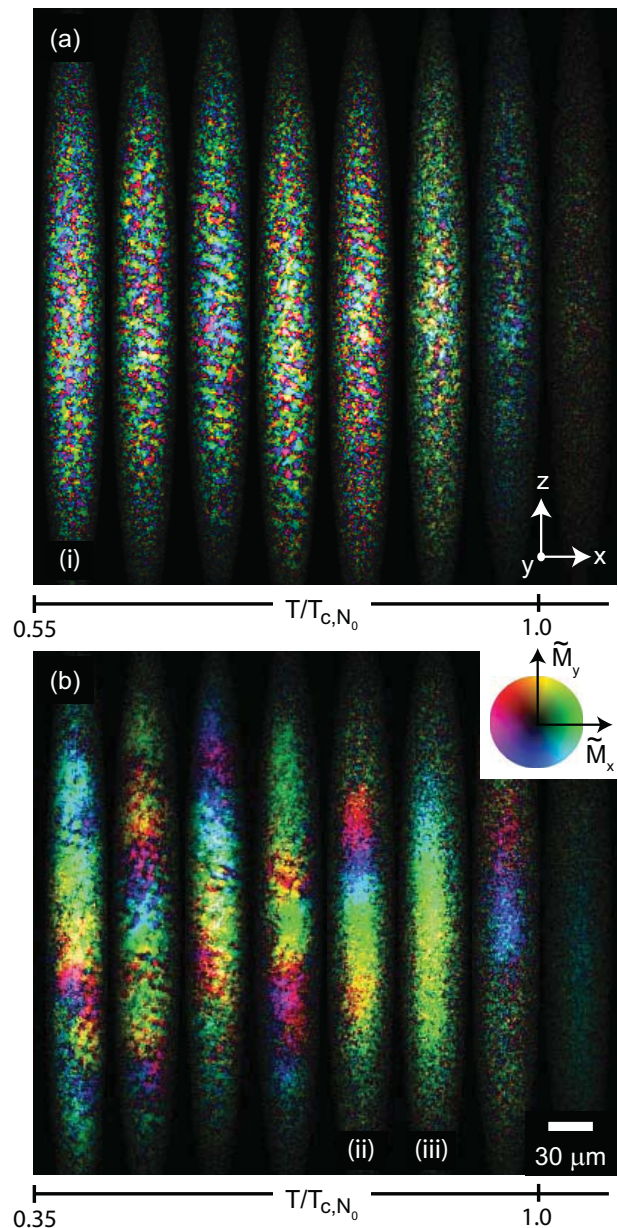


FIG. 2. Spin textures of  $^{87}\text{Rb}$   $F = 1$  spinor gases produced by cooling thermal spin mixtures with initial values (a)  $\eta = 0$  and (b)  $\eta = 1/4$ . The transverse magnetization  $\tilde{M}_{x,y}$  (color wheel shown) is shown in the  $\hat{x}$ - $\hat{z}$  plane. Temperatures are scaled by the Bose condensation temperature given the trap parameters and the population of the  $|m_z = 0\rangle$  state. Textures labeled (i), (ii) and (iii) are analyzed further in Fig. 4.

vector spins  $\vec{F} = (F_x, F_y, F_z)$  measured at each imaged pixel within  $30 \times 20 \mu\text{m}^2$  regions of the gas (Fig. 5). These regions were centered on the condensate in the  $\hat{x}$  direction while the location along  $\hat{z}$  was allowed to vary. The observed spin-space distribution was significantly prolate [27]. The local spin axis was then defined as lying along the largest-eigenvalue eigenvector of the covariance matrix  $D_{ij} = \langle (F_i - \langle F_i \rangle)(F_j - \langle F_j \rangle) \rangle$  with  $\{i, j\} \in \{x, y, z\}$ . This spin axis varies over characteristic distances of  $\simeq 50$

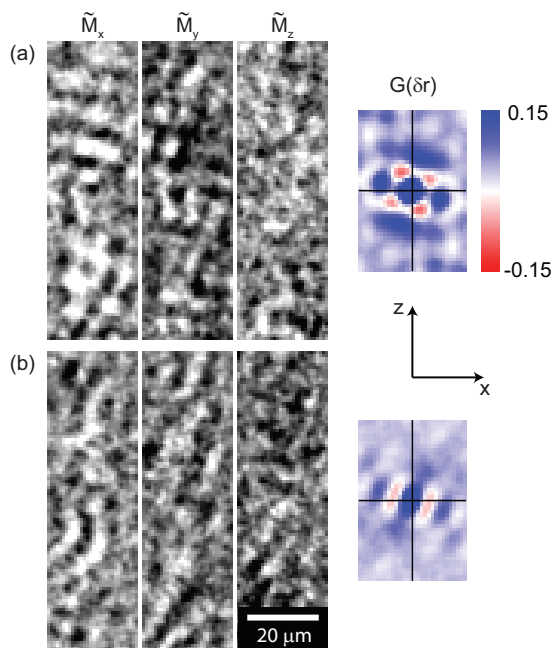


FIG. 3. The magnetization vector components  $\tilde{M}_{x,y,z}$  (grayscale spanning  $\pm 2/3$  of the maximum condensate magnetization) are shown for the central  $25 \times 100 \mu\text{m}^2$  regions of two samples produced by cooling initial mixtures with  $\eta = 0$  to 80 nK. Regions of sample (a) show prominent magnetization modulations along either a single near-vertical wavevector (top portion) or along two orthogonal wavevectors (bottom portion). In contrast, modulations in (b) are predominantly along a near-horizontal wavevector. The magnetization spatial correlation function  $G(\delta r)$  evaluated over a  $40 \times 200 \mu\text{m}^2$  region reveals patterns of alternating spins characteristic of these samples.

$\mu\text{m}$  across the length of the spin texture (Fig. 6).

### III. MAGNETIZATION TEXTURES PRODUCED FROM $\eta \neq 0$ GASES

We also studied the evolution of spin mixtures prepared with a non-zero initial quadrupole moment ( $\eta = 1/4$ ). While the small rate of spin-mixing collisions in the non-degenerate gas prevented its equilibration to  $\eta = 0$  within experimentally accessible timescales (seconds), below  $T_{c,N_0}$ , the thermal fraction of degenerate gases did reach roughly equal populations in the three Zeeman sublevels (Fig. 1), presumably due to the high density and bosonic enhancement intrinsic to a condensate. These thermal populations were all consistent with the expected non-condensate population for a quantum-degenerate, thermally equilibrated, harmonically confined Bose gas.

Yet, in spite of this condensate-mediated spin mixing, effects of the initial condition were still visible in the magnetization textures of the degenerate gas. In contrast to the case of  $\eta = 0$ , here we observe two distinct magne-

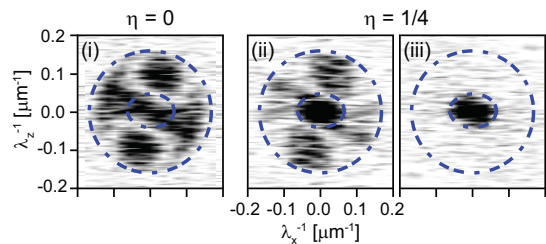


FIG. 4. Spatial Fourier power spectra of the magnetization,  $|\tilde{\mathbf{M}}(k_x, k_y)|^2$  for gases prepared with  $\eta = 0$  (i) and  $\eta = 1/4$  (ii, iii). Periodic spin modulation in (i) and (ii) is indicated by broad spectral peaks with modulation wavelength  $\lambda \simeq 10 \mu\text{m}$ . Ferromagnetic order in (ii) and (iii) is indicated by the spectral peak at zero wavevector. (ii) and (iii) correspond to gases cooled to temperatures of 100 nK and 130 nK respectively, indicating the abrupt transition to a modulated spin texture. The power spectrum is evaluated for the entire magnetization texture, corresponding to images shown in Fig. 2. Dashed ellipses show demarcation of Fourier space into the central region, indicative of ferromagnetic order, and an annular region, indicative of short-range spin modulation. Such regions are used for an empirical characterization (Fig. 7) of the spin textures.

tization patterns. Just below the condensation temperature, the spin textures showed ferromagnetic order, with a nearly uniform magnetization that varied only at long length-scales of around  $100 \mu\text{m}$ . The stability of these transverse ferromagnetic textures shows that the presence of a condensate fraction in the  $|m_z = \pm 1\rangle$  Zeeman sublevels states does not on its own guarantee the appearance of small spin domains. Only at a distinctly lower temperature does the magnetization display periodic spatial modulations. This modulation pattern coexists with ferromagnetic order, constituting a spatial variation of

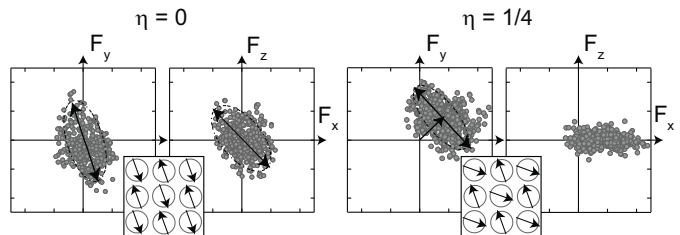


FIG. 5. The periodic magnetization textures are characterized by a spin-space axis along which the magnetization is modulated. Distributions of spins within the central  $30 \times 20 \mu\text{m}^2$  regions of the magnetization texture, for samples at the lowest temperatures. For  $\eta = 0$ , both transverse ( $F_{x,y}$ ) and longitudinal ( $F_z$ ) spin variations are evident, while for  $\eta = 1/4$  the modulation is solely transverse. The long axis of the prolate spin distribution defines the local spin axis (indicated by double-headed arrow). For  $\eta = 1/4$ , this distribution is offset due to the coexistent ferromagnetic order. Spatial patterns corresponding to the observed spin-space modulation are shown schematically at bottom. Dashed ellipses are guides to the eye.

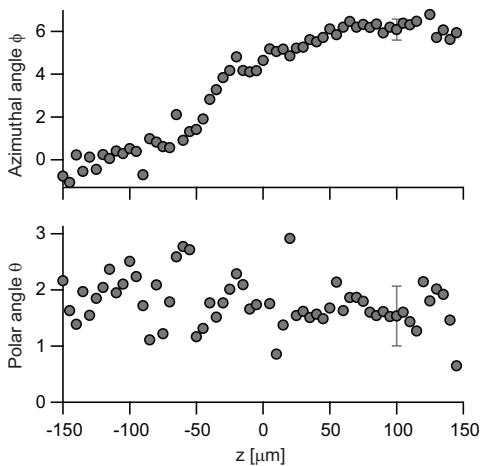


FIG. 6. The local spin axis, determined with a  $30 \mu\text{m}$  region centered variably along the  $\hat{z}$  axis, is not uniform across the extent of the condensate but meanders gradually over length scales of around  $50 \mu\text{m}$ . The azimuthal and polar angles of this axis, given in radians, with typical statistical error bar shown, are presented for the lowest-temperature sample in Fig. 2b, with initial  $\eta = 1/4$ .

the magnetization about a non-zero average value.

The distinction between long length-scale ferromagnetic order and the short length-scale spin modulation is clearly seen in the spatial Fourier power spectra of the magnetization (Fig. 4). This distinction allows us to define empirical measures of each type of spatial order. For this, we demarcate spatial Fourier space into a central region, which we may associate with ferromagnetic order, surrounded by an annular region which contains the broad spectral peaks that characterize the short length-scale spin modulation. Summing the spectral power in each of these regions provides a measure of the different magnetization patterns exhibited by the quantum gas.

These measures distinguish between spin textures obtained from differing initial conditions (Fig. 7). For gases produced with  $\eta = 0$ , the modulated spin pattern arises immediately below  $T_{c,N_0}$  and intensifies monotonically with decreasing temperature, remaining a constant fraction of the spectral power expected for a fully magnetized condensate. The ferromagnetic order remains small at all temperatures indicating that the average vector magnetization over length scales larger than  $\sim 20 \mu\text{m}$  is roughly zero. In contrast, for  $\eta = 1/4$ , ferromagnetic order dominates down to  $0.75 T_{c,N_0} = 130 \text{ nK}$ . Below this temperature, the short length-scale spin modulation emerges abruptly, as indicated by the different Fourier spectra shown in Fig. 4 (ii) and (iii), and coexists with ferromagnetism. Here we note that the magnetic dipole energy between neighboring spin domains may be approximated as  $\mu_0 \mu^2 \tilde{n}^2 l / 4\pi = k_B \times 210 \text{ nK}$ . Thus, dipolar interactions may play a role in the transition toward spatially modulated spin textures.

In addition to the presence of the two distinct magnetization patterns, the textures produced from initial

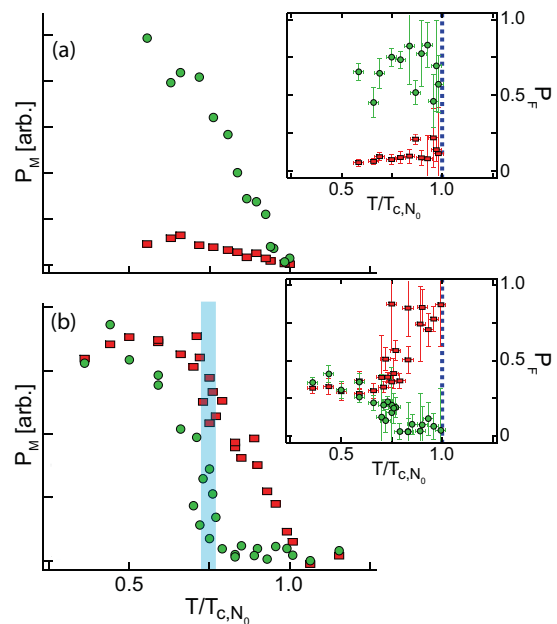


FIG. 7. Measures for ferromagnetic order (red rectangles) and for the short length-scale spin modulation (green circles) are defined as the sums  $P_M = \sum_k |\tilde{\mathbf{M}}(k_x, k_y)|^2$  in regions of spatial Fourier space defined in Fig. 4. Insets show these order parameters as fractions of the integrated spectral power expected for a uniformly magnetized condensate. (a) Gases cooled from  $\eta = 0$  show a single transition to a magnetic texture dominated by short-range spin modulation. (b) Data for  $\eta = 1/4$  show an additional transition between textures with coexistent ferromagnetic order and spin modulation observed at low temperature, and solely ferromagnetic textures observed at high temperature.

conditions  $\eta = 0$  and  $\eta = 1/4$  also differ in the overall distribution of magnetization orientations. For  $\eta = 0$ , the magnetization orientation shows no preferred axis or plane, while for  $\eta = 1/4$  the magnetization was found to lie predominantly in the (transverse)  $\hat{x}$ - $\hat{y}$  plane.

This spin-space asymmetry may be explained in part by the fact that, for  $\eta > 0$ , Bose condensation occurs first in the dominant  $|m_z = 0\rangle$  state. Transverse magnetization may then arise from the dynamical instability of this polar-state condensate [21]. This timeline for the formation of magnetization was verified by probing gases at different times during their evaporation and equilibration. Indeed, with  $\eta = 1/4$ , unmagnetized condensates in the  $|m_z = 0\rangle$  state were observed before the appearance of magnetization. Further, at  $q = h \times 70 \text{ Hz} > 2|c_2|n$ , for which the quadratic shift dominates over both the spin-dependent collisional and dipolar interactions and, thus, a  $|m_z = 0\rangle$  condensate is stable, a similar cooling sequence resulted neither in a condensate fraction in the  $|m_z = \pm 1\rangle$  states nor in the appearance of transverse magnetization.

#### IV. IMPLICATIONS FOR EQUILIBRIUM PHASES

The limited lifetime (about 1 s) of our gaseous samples restricted the duration over which they were allowed to equilibrate. This restriction raises the question as to what extent the observed magnetic textures display the characteristics of thermal equilibrium phases. To help address this question, we have verified that both the temperature and the populations of the non-condensate fractions reach equilibrium within 100 - 150 ms of the establishment of the final trap depth. Doubling the evaporation time or lengthening the equilibration period to as long as 800 ms produced no discernible changes in the magnetic order, other than overall loss in atom number. Nevertheless, as discussed above, we observe variations in the magnetization patterns in samples produced under similar conditions, and persistent differences between samples prepared from differing initial spin mixtures. These variations suggest that the magnetization of these degenerate spinor gases equilibrates only slowly, a property observed also in classical dipolar systems [28]. Therefore, the observed textures and the empirical measures used to characterize these textures cannot be considered to define the equilibrium phase of the degenerate spinor gas.

However, the presence of short-range periodic spin modulation is a robust property of the observed spin textures, appearing consistently under a variety of initial conditions. We have additionally observed similar modulation patterns following the dissolution of helical spin textures [15] as well as after long evolution times following a quench of an unmagnetized condensate to a magnetic state (at short evolution times, this instability produces a distinctly different modulation pattern) [21, 22]. This robustness, and the fact that the characteristic length-scale of the spin modulation is constant and much smaller than the extent of the gaseous sample (certainly in the  $\hat{z}$  direction), supports the claim that such structure is a characteristic of the low-temperature equilibrium configuration of the bulk quasi-two-dimensional spinor Bose gas.

We thank S.M. Girvin, T.L. Ho, J. Moore and A. Vishwanath for valuable discussions. This work was supported by the NSF, and by the DARPA OLE program (ARO Grant No. W911NF-07-1-0576). Partial personnel and equipment support was provided by the Division of Materials Sciences and Engineering, Office of Basic Energy Sciences. S.R.L. acknowledges support from NSERC and F.S. from the Gottlieb Daimler and Karl Benz Foundation.

- 
- [1] E. Kim and M. H. W. Chan, *Nature* **427**, 225 (2004).
  - [2] J. Orenstein and A. J. Millis, *Science* **288**, 468 (2000).
  - [3] J. E. Hoffman *et al.*, *Science* **295**, 466 (2002).
  - [4] G. C. Milward, M. J. Calderon, and P. B. Littlewood, *Nature* **433**, 607 (2005).
  - [5] S. Sachdev, *Science* **288**, 475 (2000).
  - [6] M. Seul and D. Andelman, *Science* **267**, 476 (1995).
  - [7] E. Dagotto, *Science* **309**, 257 (2005).
  - [8] H. Schmaljohann *et al.*, *Phys. Rev. Lett.* **92**, 040402 (2004).
  - [9] M.-S. Chang *et al.*, *Phys. Rev. Lett.* **92**, 140403 (2004).
  - [10] T.-L. Ho, *Phys. Rev. Lett.* **81**, 742 (1998).
  - [11] T. Ohmi and K. Machida, *J. Phys. Soc. Jpn.* **67**, 1822 (1998).
  - [12] S. Yi, L. You, and H. Pu, *Phys. Rev. Lett.* **93**, 040403 (2004).
  - [13] S. Yi and H. Pu, *Phys. Rev. Lett.* **97**, 020401 (2006).
  - [14] Y. Kawaguchi, H. Saito, and M. Ueda, *Phys. Rev. Lett.* **98**, 110406 (2007).
  - [15] M. Vengalattore, S. Leslie, J. Guzman, and D. Stamper-Kurn, *Phys. Rev. Lett.* **100**, 170403 (2008).
  - [16] M. Takahashi, S. Ghosh, T. Mizushima, and K. Machida, *Phys. Rev. Lett.* **98**, 260403 (2007).
  - [17] R. W. Cherng and E. Demler, *Phys. Rev. Lett.* **103**, 185301 (2009).
  - [18] Y. Kawaguchi, H. Saito, K. Kudo and M. Ueda, preprint arXiv:0909.0565 (2009).
  - [19] J. Zhang and T.-L. Ho, preprint arXiv:0908.1593 (2009).
  - [20] J. A. Kjall, A. M. Essin, and J. E. Moore, *Phys. Rev. B* **80**, 224502 (2009).
  - [21] L. Sadler *et al.*, *Nature* **443**, 312 (2006).
  - [22] S. Leslie *et al.*, *Phys. Rev. A* **79**, 043631 (2009).
  - [23] J. Kronjäger, *et al.*, preprint arXiv:0904.2339 (2009).
  - [24] J. Higbie *et al.*, *Phys. Rev. Lett.* **95**, 050401 (2005).
  - [25] M. Vengalattore *et al.*, *Phys. Rev. Lett.* **98**, 200801 (2007).
  - [26]  $G(\delta\mathbf{r})$  is accurate only over distances substantially smaller than the extent of the finite field over which it is evaluated. The correlation functions presented in Fig. 3 satisfy that criterion. Equivalently, the Fourier power spectrum is pixilated due to the finite spatial extent of the data field, and accurate measures can only be obtained for spectral features that span many pixels in Fourier space. The features shown in Fig. 4 are all broad, owing to the short-range nature of the periodic spin modulation as shown by the correlation function and in the data themselves.
  - [27] Based on numerical simulations that take into account the signal to noise ratio of the magnetization-sensitive images, the number of independent measurements within the region of interest, and assuming a gaussian noise distribution, we determined a cutoff of 1.35 for the aspect ratio of the ellipsoidal distribution (major axis radius divided by geometric mean radius) below which the spin axis was no longer well defined. This cutoff was also verified by examining the spin distributions in homogeneously magnetized condensates which did not exhibit short-range spin modulations.
  - [28] D. K. Lottis, R. M. White, and E. D. Dahlberg, *Phys. Rev. Lett.* **67**, 362 (1991).